



Thickness-dependent photocatalytic activity of bismuth oxybromide nanosheets with highly exposed (0 1 0) facets

Haiping Li^a, Tingxia Hu^b, Jianqiang Liu^c, Shue Song^d, Na Du^d, Renjie Zhang^d, Wanguo Hou^{d,*}

^a National Engineering Technology Research Center for Colloidal Materials, Shandong University, Jinan 250100, PR China

^b Environment Research Institute, Shandong University, Jinan 250100, PR China

^c School of Physics, Shandong University, Jinan 250100, PR China

^d Key Laboratory for Colloid and Interface Chemistry (Ministry of Education), Shandong University, Jinan 250100, PR China

ARTICLE INFO

Article history:

Received 4 August 2015

Received in revised form

20 September 2015

Accepted 26 September 2015

Available online 1 October 2015

Keywords:

BiOBr

Nanosheet

Thickness

Photocatalysis

Active facet

ABSTRACT

A series of BiOBr nanosheets was hydrothermally synthesized through pH adjustment of precursor suspensions. X-ray diffraction, X-ray photoelectron spectroscopy, electronic microscopy and UV–vis diffuse reflectance spectroscopy analyses indicate that these nanosheets possess similar crystallinity, surficial composition, structures, band gaps and highly exposed (0 1 0) facets, but different lateral sizes and thicknesses. The visible-light photoactivity of these nanosheets in photodegradation of salicylic acid increases with reduced nanosheet thickness. An inversely linear relationship was obtained between the pseudo-first-order rate constant (k) and the nanosheet thickness. The photoactivity enhancement of the samples with reduced nanosheet thickness is ascribed to the decreasing recombination efficiency of photogenerated charge carriers. This study indicates that the photoactivity of the BiOBr nanosheets with dominant exposed (0 1 0) facets decisively depend on the nanosheet thickness, rather than the percentage of exposed active facets ((0 0 1) facets), which may be universal for other two-dimensional photocatalysts.

© 2015 Elsevier B.V. All rights reserved.

1. Introduction

Semiconductor photocatalysis driven by the sustainable solar energy is a promising technology in solving the problems of energy crisis and environmental contamination [1–5]. On the one hand, photocatalytic water splitting to produce hydrogen and CO₂ reduction to generate hydrocarbon fuels are capable of alleviating the energy crisis. On the other hand, photocatalytic degradation of toxic pollutants can effectively remedy the environment. Nonetheless, the photoactivity of current photocatalysts is too low to satisfy the requirement of industrial applications.

Structure-performance study of semiconductor photocatalysts can provide theoretical guidance for fabricating photocatalysts with high photoactivity. Crystal facet engineering of semiconductors is an effective strategy for enhancing the photoactivity of photocatalysts [6–12]. The high photoreactivity of active crystal facets of semiconductors was traditionally thought to arise from their high surface energy [13], but recent studies indicated that the charge transfer between different facets with different energy band

structures played a more important role [14–16]. The controversy of photocatalytic mechanism in study of crystal facet engineering of semiconductors prominently resides in bismuth-based photocatalysts, especially bismuth oxyhalide (BiOX, X = Cl, Br or I) with highly exposed (0 0 1) facet. For instance, most researchers attributed the photoactivity enhancement of BiOX nanosheets to increasing exposure percentages of photoactive (0 0 1) facets [7,9,17,18]; Li et al. thought the photoactivity of Bi₃O₄Cl nanosheets with highly exposed (0 0 1) facets and similar structure as BiOX nanosheets relied on the magnitude of internal electric field (IEF) [13]; Guan et al. ascribed the higher photoactivity of BiOCl nanosheets to the more vacancy associates on the surface of (0 0 1) facets [19]. Actually, for these sheet-like photocatalysts with highly exposed (0 0 1) facets, a prominent reduction of nanosheet thickness was observed along with the increase of the (0 0 1) facet exposure percentage [7,9,17,18], the IEF magnitude [13] or the vacancy associate amount [19]. Recently, we investigated the relationship between the photoactivity of BiOBr lamellas and the lamella thickness and found that the photoactivity of the samples depended inversely proportionally on the lamella thickness [20]. Whether this inversely proportional relationship applies universally to two-dimensional (2D) semiconductor photocatalysts is unknown yet. Besides, the (0 0 1) facet exposure percentages of reported BiOX samples with

* Corresponding author. Fax: +86 531 88364750.
E-mail address: wghou@sdu.edu.cn (W. Hou).

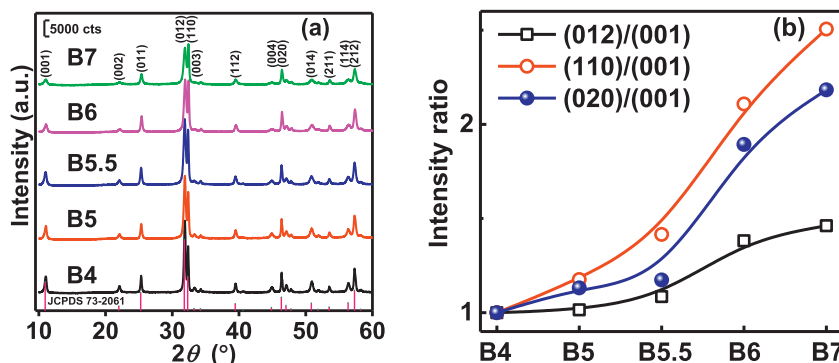


Fig. 1. (a) XRD patterns and (b) peak intensity ratios of BiOBr samples. All the ratios were normalized by those of B4.

highly exposed (001) facets were all quite large ($\geq 70\%$) and varied along with the change of the IEF magnitude [13], the vacancy associate amount [19] or the lamella thickness [20]. Investigation on the effect of a certain factor on the photoactivity of these samples by controlling variate method is difficult, but it's possible and essential to further confirm the inversely proportional dependence of the photoactivity of 2D semiconductors on the nanosheet thickness by preparing a series of 2D photocatalysts with considerably different nanosheet thickness but little changing exposed active facet percentage, vacancy amount, IEF magnitude, etc.

In this work, we investigate the dependence of the photoactivity of BiOBr nanosheets with highly exposed (010) facets on the nanosheet thickness. A linear photoactivity enhancement of the samples is confirmed with decreased nanosheet thickness, which reveals that the nanosheet thickness rather than the exposed active facet ((001) facet) percentage has a decisive effect on the photoactivity of the BiOBr nanosheets.

2. Experimental

2.1. Materials

$\text{Bi}(\text{NO}_3)_3 \cdot 5\text{H}_2\text{O}$, NaBr, NaOH, and salicylic acid were of A.R. grade, purchased from Aladdin (Shanghai, PR China) and used without further purification. Water used in experiments with resistivity of $18.2 \text{ M}\Omega \text{ cm}$ was obtained from a Hitech-Kflow water purification system (Hitech, Shanghai, PR China).

2.2. Preparation of BiOBr nanosheets

BiOBr nanosheets were synthesized as reported with minor modifications [8,21]. Specifically, 0.02 mol of $\text{Bi}(\text{NO}_3)_3 \cdot 5\text{H}_2\text{O}$ and 0.02 mol of NaBr were dispersed in 300 mL water under stirring for 30 min. The dispersion was divided equally into five parts. Aqueous NaOH (1 mol/L) was added dropwise to the dispersions, to adjust their pH values to 4.0, 5.0, 5.5, 6.0 and 7.0, respectively. Then the resulting dispersions were transferred into 100-mL autoclaves and heated at 160°C for 24 h. Finally, the precipitates were collected by filtration, washed thoroughly with water, and dried at 60°C in an oven. The BiOBr samples obtained at pH 4.0, 5.0, 5.5, 6.0 and 7.0 were denoted as B4, B5, B5.5, B6 and B7, respectively.

2.3. Characterization

Powder X-ray diffraction (XRD) was implemented on a X'Pert Pro MPD X-ray diffractometer (Philips, Holland), with $\text{Cu K}\alpha$ radiation ($\lambda = 1.54184 \text{ \AA}$) generated at 40 mA and 40 kV and at a scanning rate of $1^\circ/\text{min}$. The crystalline size perpendicular to the reflection plane was calculated using Scherrer formula with the instrument width of 0.05° . X-ray photoelectron spectroscopy (XPS) was per-

formed on a Thermo Scientific Escalab 250Xi spectrometer (UK) with $\text{Al K}\alpha$ radiation. The C 1s peak at 284.6 eV was used to calibrate peak positions. Morphology observation was carried out on a Supra55 field emission-scanning electron microscope (SEM, Zeiss, USA) and a JEM-2100F transmission electron microscope (TEM, Jeol, Japan). The elemental composition and contents of samples were investigated by an energy dispersive X-ray spectrometer (EDS) equipped on the SEM. Selected area electron diffraction (SAED) patterns were obtained on the TEM. UV-vis diffuse reflectance spectra (UV-vis DRS) were obtained using a U-4100 spectrophotometer (Hitachi, Japan), with a BaSO_4 reference. Photoluminescence (PL) spectra were measured using an F-7000 spectrophotometer (Hitachi, Japan) with an excitation wavelength of 300 nm. The excitation and emission slit widths were set at 5 and 10 nm, respectively. Time-resolved fluorescence decay spectra were measured on an Edinburgh Analytical Instruments FLS920 time-resolved spectrofluorometer (UK) using the time-correlated single photon counting method and excited with a picosecond pulsed diode laser (EPL-375) at 377.8 nm. Specific surface areas were probed by measuring volumetric N_2 adsorption-desorption isotherms at liquid nitrogen temperature, using a Quantachrome NOVA2000E instrument (USA). Samples were degassed at 120°C for 6 h under vacuum before measurements.

The photocatalytic performance of as-prepared photocatalysts under visible light irradiation was evaluated by degrading salicylic acid (SA) at room temperature, on a XPA-7 photocatalytic reaction apparatus (Xujiang Electromechanical Plant, Nanjing, PR China) [22] (Fig. S1, Supporting information). A 400 W metal halide lamp equipped with an ultraviolet cutoff filter ($\lambda \geq 420 \text{ nm}$) was used as the visible light source. The distance between the lamp and reaction tubes containing 50 mL of SA (20 mg/L) solution and 0.05 g of BiOBr samples is about 10 cm. A water filter around the lamp is used to adsorb the infrared light. The reaction tubes around the lamp are all soaked in a constant temperature bath ($\sim 22^\circ\text{C}$). The photoabsorption surface area of each reaction tube is approximately equal to half of the side surface area of reaction tubes, i.e., $\sim 45 \text{ cm}^2$. Prior to irradiation, the suspension was treated by ultrasonication for 5 min and then stirred in the dark for 1 h, to ensure sorption equilibrium. All the reaction tubes rotated around the lamp at a constant rate to assure the same photoabsorption of all the suspensions when the lamp was turned on. After a given irradiation time, $\sim 4 \text{ mL}$ aliquots were collected and filtered through $0.45\text{-}\mu\text{m}$ nylon syringe filters. The absorbance of filtrates was measured by a Hewlett-Packard 8453 UV-vis spectrophotometer (USA) at a wavelength of 296 nm. The ratio of remaining SA concentration to its initial concentration, C/C_0 , was obtained by calculating the ratio of the corresponding absorbance. Total organic carbon (TOC) contents were measured by a TOC analyzer (Shimadzu TOC-L CPN CN200, Japan).

Table 1
Physicochemical properties and photocatalytic efficiencies of BiOBr samples.

Sample	D^a (nm)	L^b (nm)	H^c (nm)	$F_{(010)}^d$ (%)	S_{BET}^e ($m^2 g^{-1}$)	$10^3 k^f$ (h^{-1})	$10^3 k'^g$ ($g m^{-2} h^{-1}$)
B4	92	207	60	53	19.9	37.4	1.88
B5	79	120	55	43	12.5	40.9	3.27
B5.5	65	101	51	44	13.8	45.3	3.28
B6	61	134	44	52	16.4	47.3	2.88
B7	50	372	36	79	15.3	51.1	3.34

^a Average nanosheet thickness calculated using Scherrer formula.

^b Average nanosheet length.

^c Average nanosheet thickness from SEM results.

^d Exposure percentage of (0 1 0) facet.

^e BET specific surface area.

^f Pseudo-first kinetics rate constant of photodegradation of salicylic acid.

^g k normalized by S_{BET} .

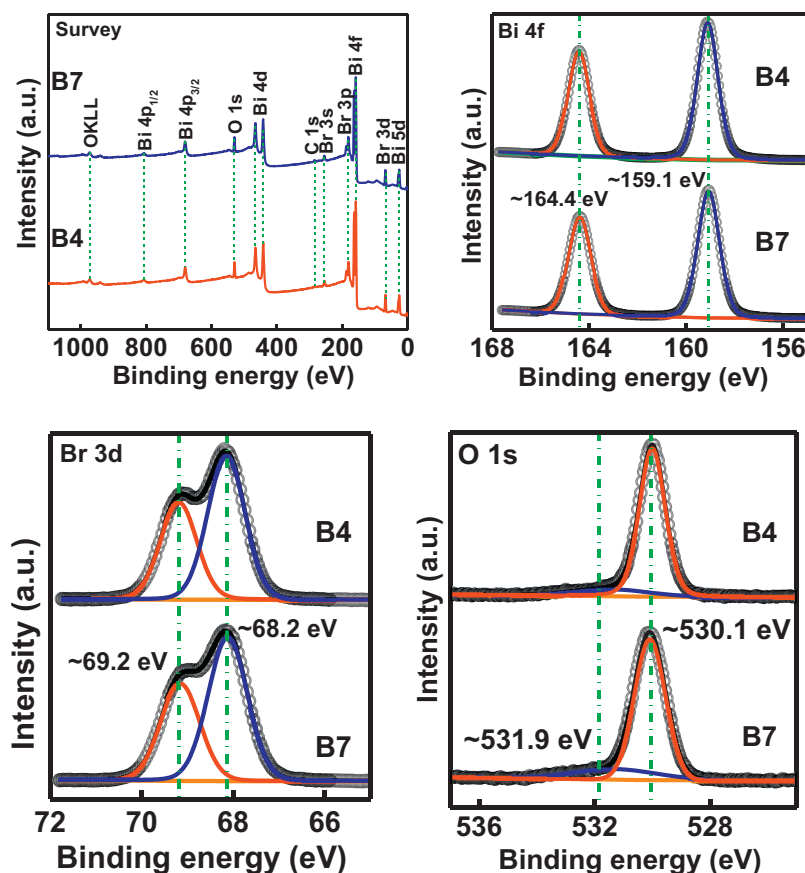


Fig. 2. XPS survey spectra and high resolution XPS spectra of Bi 4f, Br 3d and O 1s regions for BiOBr samples. Numbers in the figure are binding energies of relative peaks.

3. Results and discussion

3.1. Characterization

XRD patterns of the samples are shown in Fig. 1a. They exhibit similar diffraction peak positions which are indexed to a pure tetragonal phase of BiOBr (JCPDS No. 73-2061), and similar peak intensity except (0 0 1) peak, indicating similar crystallinity of the samples. The weakened (0 0 1) peaks with increasing reaction pH (Fig. 1a), clearly shown by the increasing intensity ratios of (0 1 2), (1 1 0) and (0 2 0) to (0 0 1) peaks (Fig. 1b) demonstrates the reduced exposure percentage of (0 0 1) facets. The average crystallite sizes (D) along the b -axis of the samples were calculated using the Scherrer formula [23,24]: $D = 0.89\lambda / (B \cos\theta)$, where λ , B , and θ are the Cu $K\alpha$ wavelength, the full width at half-maximum intensity (FWHM) of (0 2 0) peak minus the instrumental width (Fig. S2, Supporting

information) in radians, and the Bragg's diffraction angle, respectively. It decreases from ~92 to ~50 nm with increasing reaction pH (Table 1).

XPS measurement (Fig. 2) was used to confirm the elemental composition and atomic chemical microenvironment. The survey spectra indicate that both B4 and B7 contain Bi, Br and O elements. The C 1s peaks result from adventitious carbon [25]. The high-resolution Bi 4f, Br 3d and O 1s spectra of the samples all exhibit similar peak positions (as shown by the dashed lines), indicating similar chemical microenvironments of atoms. The Bi 4f and Br 3d spectra were both perfectly deconvoluted into two peaks, corresponding to Bi 4f_{5/2} and 4f_{7/2}, and Br 3d_{5/2} and 3d_{3/2}, respectively. Peaks at binding energies of ~164.4 and ~159.1 eV in the Bi 4f high-resolution spectra correspond to 4f_{5/2} and 4f_{7/2} of Bi³⁺ in BiOBr, respectively. In the Br 3d high-resolution spectra, peaks at binding energies of ~69.2 and ~68.2 eV are ascribed to 3d_{5/2} and 3d_{3/2}

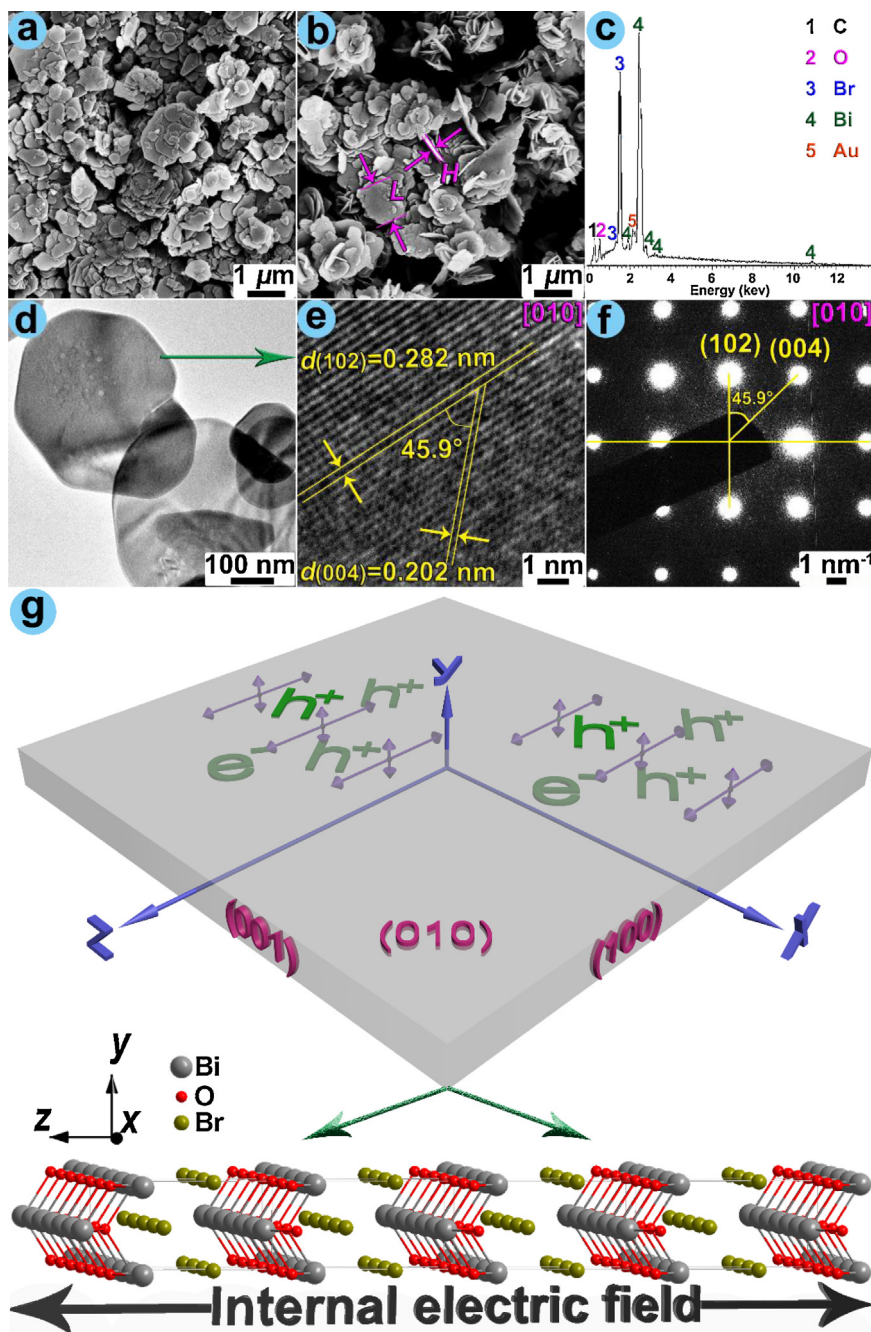


Fig. 3. SEM images of (a) B4 and (b) B7, (c) EDS, (d) TEM, (e) HRTEM and (f) SAED images of B4, and (g) schematic illustrations of BiOBr nanosheet with transfer directions of photogenerated electrons and holes and its crystal structure.

of Br^- in BiOBr, respectively. In the O 1s high resolution spectra, peaks at ~ 530.1 and $\sim 531.9 \text{ eV}$ are attributed to O in the BiOBr and other components (such as $-\text{OH}$ and H_2O) adsorbed on the surface of BiOBr, respectively [26].

SEM and TEM images show the sheet-like structures of the samples (Figs. 3a, b, d, S3 and S4a, Supporting information). Energy dispersion X-ray spectroscopy (EDS) analysis (Fig. 3c) reveals that the samples contain Bi, Br and O elements, similar to the XPS result, with molar ratio of 1.08/1.02/1 which is close to the theoretical value. C and Au are ascribed to conductive adhesive and sputtered gold before observation, respectively. High-resolution TEM image of B4 show two sets of lattice fringes with an angle of 45.9° and the spacings of 0.282 and 0.202 nm (Fig. 3e), respectively, corresponding to (102) and (004) facets both of which

are perpendicular to (010) facet of BiOBr crystal. Selected area electron diffraction (SAED) pattern shows clear ordered diffraction spots (Fig. 3f), indicating a single crystal nanosheet and that all the diffraction planes are perpendicular to the (010) facet. B7 shows similar HRTEM and SAED results as B4 (Fig. S4b, c). Based on these results, it's concluded that the BiOBr nanosheets are exposed with (010) facets on both the top and the bottom surfaces and with (001) and (100) facets on the lateral surfaces (Fig. 3g), which is in accordance with the reported result [21]. The XRD, TEM and SAED results demonstrate that the D is the average thickness of the single crystal nanosheets. Lateral sizes (L) of more than one thousand of nanosheets of the samples were measured (Fig. S5, Supporting information). Their average L values are $\sim 101\text{--}372 \text{ nm}$ and decrease then increase with increasing reaction pH (Table 1).

The average thicknesses (H) of the samples obtained by measuring more than one hundred of nanosheets (Fig. S6, Supporting information) were ~ 36 – 60 nm (Table 1). Nearly all the thicknesses of the nanosheets are <100 nm (Fig. S6), indicating the use of Scherrer formula is reasonable [27,28]. The H exhibits similar trend as the D with increasing reaction pH (Table 1), but the latter is more precise because of the extreme nonuniformity of the nanosheet thickness (Fig. S6). The decrease of D with increasing pH arises probably from the increasing exposure percentages of (010) facets and decreasing exposure percentages of (001) facets. This is because with increasing pH, the H^+ ions adsorbed on the O-terminated (001) facets become fewer, which is not favorable for the exposure of (001) facet with high energy [21]. Assuming the top and bottom planes of BiOBr nanosheets are square (Fig. 3g), the percentages of exposed (010) facets ($F_{(010)}$) of the samples were figured out using the equation $F_{(010)} = 1/(1 + 2D/L)$. $F_{(010)}$ values of the samples are all $>43\%$ and exhibit a decrease followed by an increase with increasing reaction pH (Table 1). Thus, the percentage of exposed (001) facets ($F_{(001)}$) of the samples probably decreases gradually with increasing reaction pH and is $\ll 57\%$ (considering the exposures of (102), (110), and (100) facets) (Table 1 and Figs. 1, 3 e,f and S4b,c), which agrees well with the XRD results.

Photoabsorption capability is an important factor influencing the photocatalytic performance of photocatalysts [2,29], and is usually evaluated using the UV–vis DRS. As shown in Fig. 4, all the BiOBr samples show similar absorption in the visible light region. The energy band gaps of the samples can be calculated using equation: $\alpha h\nu = A(h\nu - E_g)^{n/2}$, where α , ν , A , and E_g are the absorption coefficient, the light frequency, the proportionality constant, and the energy band gap, respectively. The value of n depends upon the characteristics of transition in the semiconductor ($n=1$ and 4 for directly and indirectly allowed transitions, respectively). For the current BiOBr samples, $n=4$ is obtained by Parida's method [30]. The determined E_g values of the BiOBr samples are very close, i.e., 2.76 ± 0.01 eV (Inset in Fig. 4).

Specific surface areas of photocatalysts also affect the photoactivity of semiconductor photocatalysts [31]. Fig. 5a show N_2 sorption isothermal curves of the samples. All curves show a type

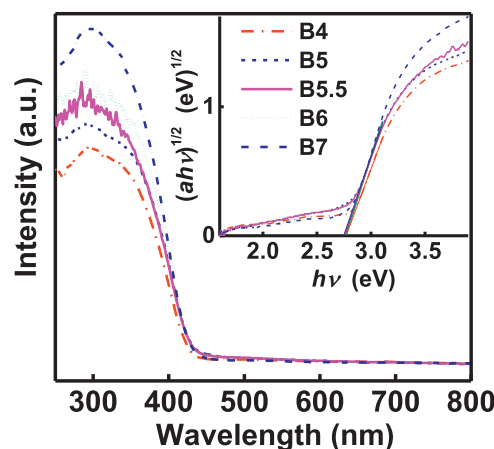


Fig. 4. UV–vis diffuse reflectance spectra of BiOBr samples. Inset is the $(\alpha h\nu)^{1/2}$ vs. $h\nu$ curves.

IV isotherm and H3 hysteresis loop, revealing the formation of slit-shaped pores [32] by stacking of the BiOBr nanosheets. Their pore size distribution curves from the adsorption branch (Fig. 5b) indicate that the samples have similar mesopore size (2.6 ± 0.3 nm). The Brunauer–Emmett–Teller specific surface areas (S_{BET}) of the samples are approximately equal, being 12.5 – 19.9 $m^2 g^{-1}$, as shown in Table 1.

3.2. Photocatalytic activity

Photocatalytic activity of the BiOBr samples are investigated by degrading salicylic acid (SA) under visible light ($\lambda \geq 420$ nm) irradiation. SA shows no photoabsorption in visible light region (Fig. S7, Supporting information), and adsorbed percentages of SA on the BiOBr samples are $<3\%$ after reaching sorption equilibrium (Fig. S8, Supporting information), indicating that the photosensitization [1] and adsorption amount effects on the photodegradation process are negligible. Thus, SA is an ideal choice to evaluate the photoactivity

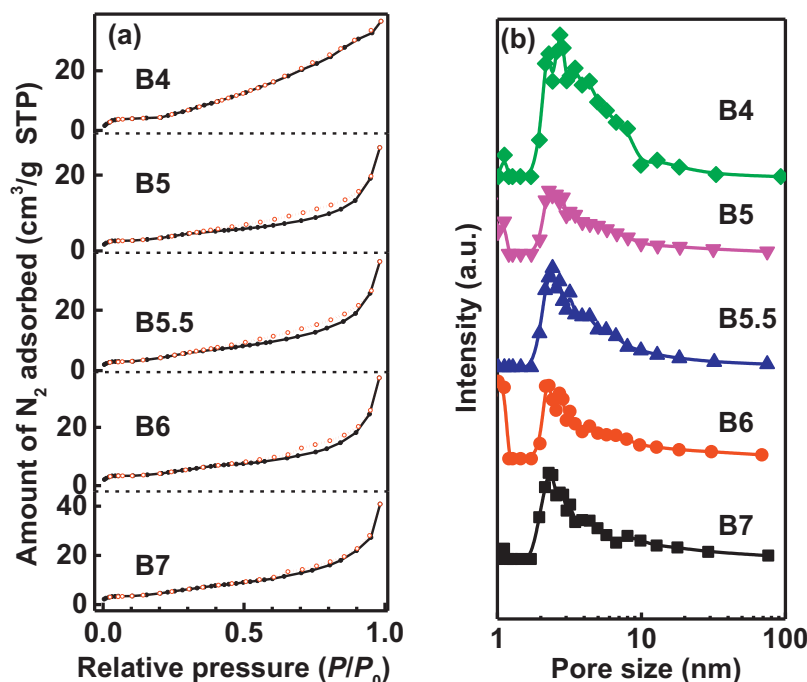


Fig. 5. (a) N_2 sorption isothermal and (b) pore size distribution curves for BiOBr nanosheets.

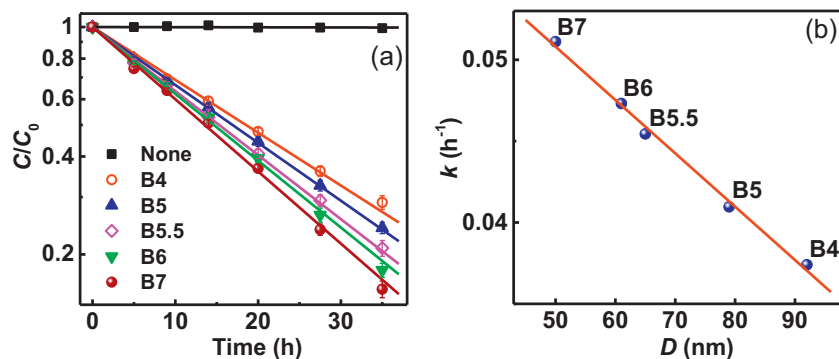


Fig. 6. (a) Photodegradation of salicylic acid on BiOBr samples under visible light irradiation and (b) variation of pseudo-first-order kinetics rate constant (k) with average nanosheet thickness (D) of the samples. The solid lines are obtained by fitting the data to (a) a pseudo-first order kinetics model and (b) a linear model.

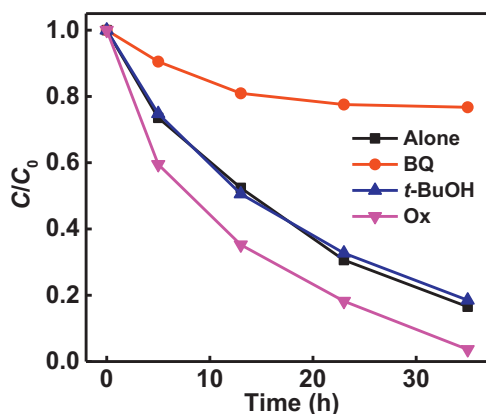


Fig. 7. Photocatalytic degradation of SA on the sample B7 with different scavengers: 40 mM *tert*-butyl alcohol (*t*-BuOH), 0.4 mM sodium oxalate (Ox), and 0.2 mM benzoquinone (BQ).

of the BiOBr samples under visible light irradiation. The absorbance of the SA hardly varies in 35 h without the photocatalysts (Fig. 6a) or the light irradiation (Fig. S9, Supporting information), meaning that both the photocatalysts and the light illumination are the prerequisites for photodegradation of the SA. As shown in Fig. 6a, the samples from B4 to B7 exhibit a gradually enhanced photocatalytic efficiency. After 35 h, the B4 and B7 photodegraded ~ 71 and $\sim 85\%$ of the SA, respectively. TOC results also show that the mineralization rate of the SA on the B7 is higher than that on the B4. After 35 h, the SA is mineralized by ~ 36 and $\sim 50\%$ on the B4 and B7, respectively (Fig. S10, Supporting information).

To quantitatively compare the photoactivity of the BiOBr samples, the photodegradation data were fitted with a pseudo-first-order kinetics equation: $-\ln(C/C_0) = kt$, where t , k , C , and C_0 are the degradation time, the apparent first-order rate constant, the SA concentrations at t and $t = 0$, respectively (Fig. 6a and Table S1, Supporting information). The k of the samples increases monotonously with increasing reaction pH, and the k of B7 is ~ 0.5 times larger than that of B4 (Table 1). To exclude the influence of the S_{BET} , the k normalized by the S_{BET} (k') was figured out. It exhibits a basically similar trend as the k with increasing reaction pH (Table 1).

Roles of active species in the photodegradation process were tested by adding individual scavenger to the photodegradation suspensions, using sample B7 as an example. The scavengers used were *tert*-butyl alcohol (*t*-BuOH) for $\bullet\text{OH}$, sodium oxalate (Ox) for holes (h^+) [33], and benzoquinone (BQ) for $\bullet\text{O}_2^-$ [30]. Fig. 7 shows that the addition of *t*-BuOH causes no change in the photodegradation efficiency of B7, indicating $\bullet\text{OH}$ is not a significant active species in the photocatalytic process. A significant suppression of photocatalytic

performance is observed when BQ is added, confirming the important role of $\bullet\text{O}_2^-$. The addition of Ox induces a prominent increase of photocatalytic efficiency, which is because the Ox consumes the h^+ , decreasing the recombination efficiency of e^- and h^+ and more electrons are left to generate $\bullet\text{O}_2^-$, further demonstrating $\bullet\text{O}_2^-$ is a significant active species in the photocatalytic process. Thus, the photocatalytic process is mainly governed by $\bullet\text{O}_2^-$.

3.3. Thickness-dependence of photoactivity

Similar visible light absorption and band gaps of the BiOBr nanosheets demonstrate that the photoabsorption is not a key factor resulting in a difference in their photoactivity. The similar trend of the k' as the k with increasing reaction pH indicates that the S_{BET} is not a key factor either. In addition, similar crystallinity (Fig. 1a) and surficial structure of the samples (Fig. 3), as discussed above, mean that none of these factors causes the difference in photoactivity of the samples. The effect of $F_{(010)}$ on the photoactivity difference should be negligible because the k shows an increase trend with increasing $F_{(010)}$ (Fig. S11a, Supporting information) or likely decreasing $F_{(010)}$ (Fig. 1b). The k shows no regular change with increasing L (Fig. S11b), demonstrating that the L doesn't cause the photoactivity difference of samples either. Therefore, the photoactivity of the samples are likely dependent on the fine variation of the D .

The k decreases linearly with increasing D (Fig. 6b), complying with the equation $k = -0.00066D + 0.077$. The k vs. H curve shows a similar linear trend (Fig. S12, Supporting information). The linear relationship evidently verifies the decisive influence of the nanosheet thickness on the photoactivity of samples. Furthermore, we also analyzed the photocatalytic data of BiOBr [7,20], BiOCl [17], and $\text{Bi}_2\text{O}_3\text{Cl}$ [13] nanosheets in the literature, and a similar linear relationship was obtained for these literature samples (Fig. S13, Supporting information), although the literature authors ascribed their photoactivity enhancement to either the increasing exposure percentages of photoactive facets or the intensifying IEF. In association with our previous results about the linear dependence of the k on the nanosheet thickness for the BiOBr lamellas with highly exposed (001) facets [20], we can conclude that this inversely linear dependence of the k on the nanosheet thickness is irrelevant to the exposed facets of the nanosheets. Thus, the nanosheet thickness is a crucial factor influencing the photoactivity of 2D semiconductor photocatalysts.

The BiOBr nanosheets with $D < 92$ nm can be wholly excited by the used visible light because the penetration depth of visible light in semiconductors are generally > 100 nm [34–36]. The decrease of particle size can reduce the migration time of photogenerated electrons (e^-) and holes (h^+) from the interior to the surface of

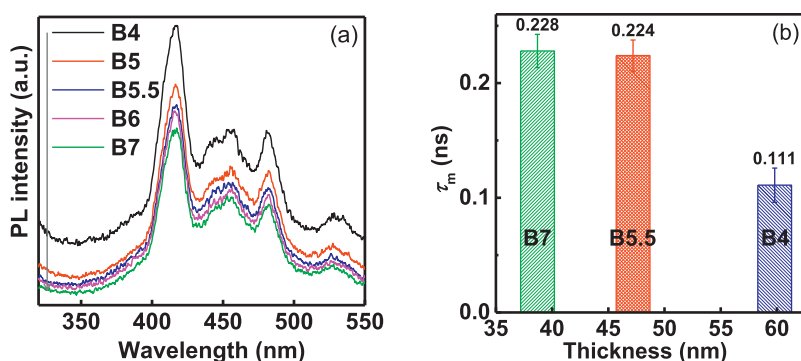


Fig. 8. (a) Photoluminescence (PL) spectra of BiOBr samples and (b) variation of their average PL lifetimes (τ_m) with nanosheet thickness (D).

particles and is thus favorable for the decrease of their recombination efficiency [37,38]. For the BiOX nanosheets, the self-generated IEF along the c -axis improves the separation of photoinduced e^- and h^+ [31,39] and accelerates the movements of e^- along the c -axis [8,13,39], which was considered as the reason for the photoactivity enhancement of BiOX nanosheets with increasing $F_{(001)}$ [7,9,17,18]. Nonetheless, the transfer of h^+ need not be on the contrary direction [13,40]. We think that the h^+ may also transfer along the $[Bi_2O_2]$ layers or the b -axis (Fig. 3g). In this case, the reduced D alone the b -axis (Fig. 3g) can decrease the migration distance of h^+ and thus the bulk recombination of e^- and h^+ , favorable for the photoactivity enhancement of the BiOX nanosheets.

Photoluminescence (PL) intensity and lifetime of photocatalysts are capable of characterizing indirectly the recombination efficiency of photogenerated e^- and h^+ [13,29,41,42]. PL spectra of the BiOBr samples with an excitation wavelength of 300 nm shows that the PL intensity of samples decreases gradually with reduced D (Fig. 8a), indicating the decreasing recombination efficiency of e^- and h^+ . The time-resolved PL decay spectra of B4, B5.5 and B7 were performed with an excitation wavelength of 377.8 nm and a monitoring wavelength of 416 nm. These decay spectra all exhibit a multi-exponential decay process and can be well fitted to a three-exponential model (Fig. S14 and Table S2, Supporting information). A gradual increase of average PL lifetime (τ_m) with reduced D (Fig. 8b) suggests the decrease of the recombination efficiency of e^- and h^+ , which accords with the PL spectrum results.

In this work, the prepared BiOBr nanosheets all highly expose (010) facets, and in our previous work [20], they all highly expose (001) facets. Under these two circumstances, the changes of exposure percentages of photoactive (001) facets with varying nanosheet thicknesses are relatively little, which is probably why the influence of the nanosheet thickness dominates over that of the (001) facet exposure percentage on the photoactivity. This study indicates that the nanosheet thickness is an important factor influencing the photoactivity of two-dimensional semiconductors and should be paid much attention to in research about photocatalytic mechanism.

4. Conclusions

A series of BiOBr nanosheets with highly exposed (010) facets and different D values were successfully prepared via a pH adjustment of reaction dispersions. Effect of the D on the photoactivity was investigated, and an inversely linear relationship between k and D was obtained. This inversely linear relationship also works well for the BiOCl and Bi_3O_4Cl nanosheets in the literature, and thus is probably universal for 2D semiconductor photocatalysts. It should be paid much attention to in studies of photocatalytic mechanism.

Acknowledgements

This work was supported financially by the National Natural Science Foundation of China (No. 21173135 and 21273135) and the Fundamental Research Funds of Shandong University in China (No. 13220075614004).

Appendix A. Supplementary data

Supplementary data associated with this article can be found, in the online version, at <http://dx.doi.org/10.1016/j.apcatb.2015.09.050>.

References

- [1] C. Chen, W. Ma, J. Zhao, *Chem. Soc. Rev.* 39 (2010) 4206–4219.
- [2] S.J.A. Moniz, S.A. Shevlin, D.J. Martin, Z.-X. Guo, J. Tang, *Energy Environ. Sci.* 8 (2015) 731–759.
- [3] H. Li, Y. Zhou, W. Tu, J. Ye, Z. Zou, *Adv. Funct. Mater.* 25 (2015) 998–1013.
- [4] C. Li, G. Chen, J. Sun, Y. Feng, J. Liu, H. Dong, *Appl. Catal. B* 163 (2015) 415–423.
- [5] C. Li, G. Chen, J. Sun, Y. Feng, H. Dong, Z. Han, Y. Hu, C. Lv, *New J. Chem.* 39 (2015) 4384–4390.
- [6] G. Liu, J.C. Yu, G.Q. Lu, H.-M. Cheng, *Chem. Commun.* 47 (2011) 6763–6783.
- [7] D. Zhang, J. Li, Q. Wang, Q. Wu, *J. Mater. Chem. A* 1 (2013) 8622–8629.
- [8] J. Jiang, K. Zhao, X. Xiao, L. Zhang, *J. Am. Chem. Soc.* 134 (2012) 4473–4476.
- [9] L. Ye, L. Tian, T. Peng, L. Zan, *J. Mater. Chem.* 21 (2011) 12479–12484.
- [10] M. Pan, H. Zhang, G. Gao, L. Liu, W. Chen, *Environ. Sci. Technol.* 49 (2015) 6240–6248.
- [11] C. Li, C. Koenigsmann, W. Ding, B. Rudsteyn, K.R. Yang, K.P. Regan, S.J. Konezny, V.S. Batista, G.W. Brudvig, C.A. Schmuttenmaer, J.H. Kim, *J. Am. Chem. Soc.* 137 (2015) 1520–1529.
- [12] H. Li, H. Yu, X. Quan, S. Chen, H. Zhao, *Adv. Funct. Mater.* 25 (2015) 3074–3080.
- [13] J. Li, L. Zhang, Y. Li, Y. Yu, *Nanoscale* 6 (2014) 167–171.
- [14] T. Tachikawa, S. Yamashita, T. Majima, *J. Am. Chem. Soc.* 133 (2011) 7197–7204.
- [15] Z. Zheng, B. Huang, J. Lu, X. Qin, X. Zhang, Y. Dai, *Chem. Eur. J.* 17 (2011) 15032–15038.
- [16] L. Zhang, J. Shi, M. Liu, D. Jing, L. Guo, *Chem. Commun.* 50 (2014) 192–194.
- [17] L. Ye, L. Zan, L. Tian, T. Peng, J. Zhang, *Chem. Commun.* 47 (2011) 6951–6953.
- [18] L. Ye, J. Chen, L. Tian, J. Liu, T. Peng, K. Deng, L. Zan, *Appl. Catal. B* 130–131 (2013) 1–7.
- [19] M. Guan, C. Xiao, J. Zhang, S. Fan, R. An, Q. Cheng, J. Xie, M. Zhou, B. Ye, Y. Xie, *J. Am. Chem. Soc.* 135 (2013) 10411–10417.
- [20] H. Li, J. Liu, X. Liang, W. Hou, X. Tao, *J. Mater. Chem. A* 2 (2014) 8926–8932.
- [21] W. Lin, X. Wang, Y. Wang, J. Zhang, Z. Lin, B. Zhang, F. Huang, *Chem. Commun.* (2014), <http://dx.doi.org/10.1039/c40133cc41498a>.
- [22] H. Li, Q. Deng, J. Liu, W. Hou, N. Du, R. Zhang, X. Tao, *Catal. Sci. Technol.* 4 (2014) 1028–1037.
- [23] A. Jahel, C.M. Ghimbeu, A. Darwiche, L. Vidal, S. Hajjar-Garreau, C. Vix-Guterl, L. Monconduit, *J. Mater. Chem. A* 3 (2015) 11960–11969.
- [24] Q. Li, B. Guo, J. Yu, J. Ran, B. Zhang, H. Yan, J.R. Gong, *J. Am. Chem. Soc.* 133 (2011) 10878–10884.
- [25] M. Zhang, C. Shao, J. Mu, X. Huang, Z. Zhang, Z. Guo, P. Zhang, Y. Liu, *J. Mater. Chem.* 22 (2012) 577–584.
- [26] X. Shi, X. Chen, X. Chen, S. Zhou, S. Lou, Y. Wang, L. Yuan, *Chem. Eng. J.* 222 (2013) 120–127.
- [27] Z. Yang, Y. Huang, G. Chen, Z. Guo, S. Cheng, S. Huang, *Sens. Actuators B* 140 (2009) 549–556.
- [28] Q. Wang, N. Wang, S. He, J. Zhao, J. Fang, W. Shen, *Dalton Trans.* (2015), <http://dx.doi.org/10.1039/C5DT01762A>.
- [29] H. Li, W. Hou, X. Tao, N. Du, *Appl. Catal. B* 172–173 (2015) 27–36.

- [30] L. Mohapatra, K. Parida, M. Satpathy, *J. Phys. Chem. C* 116 (2012) 13063–13070.
- [31] H. Cheng, B. Huang, Y. Dai, *Nanoscale* 6 (2014) 2009–2026.
- [32] J.L. Gunjaker, I.Y. Kim, J.M. Lee, N.S. Lee, S.J. Hwang, *Energy Environ. Sci.* 6 (2013) 1008–1017.
- [33] X. Xiao, R. Hu, C. Liu, C. Xing, C. Qian, X. Zuo, J. Nan, L. Wang, *Appl. Catal. B* 140–141 (2013) 433–443.
- [34] V. Smolyaninova, E. Talanova, R. Kennedy, R.M. Kolagani, M. Overby, L. Aldaco, G. Yong, K. Karki, *Phys. Rev. B* 76 (2007) 104423.
- [35] D.V. Palanker, G.M. Knippels, T.I. Smith, H.A. Schwettman, *Opt. Commun.* 148 (1998) 215–220.
- [36] R.K. Kim, B.K. Cha, S. Jeon, C.-W. Seo, S. Yun, *J. Korean Phys. Soc.* 65 (2014) 446–449.
- [37] C. Pan, Y. Zhu, *J. Mater. Chem.* 21 (2011) 4235–4241.
- [38] H. Yin, T. Tsuzuki, K.R. Millington, P.S. Casey, *J. Nanopart. Res.* 16 (2014) 2641.
- [39] J. Li, Y. Yu, L. Zhang, *Nanoscale* 6 (2014) 8473–8488.
- [40] R. Li, F. Zhang, D. Wang, J. Yang, M. Li, J. Zhu, X. Zhou, H. Han, C. Li, *Nat. Commun.* 4 (2013) 1432.
- [41] H. Li, J. Liu, W. Hou, N. Du, R. Zhang, X. Tao, *Appl. Catal. B* 160–161 (2014) 89–97.
- [42] X. Wang, C. Liow, A. Bisht, X. Liu, T.C. Sum, X. Chen, S. Li, *Adv. Mater.* 27 (2015) 2207–2214.